Ceilometer based analysis of Shanghai's boundary layer height (under rain and fog free conditions)

Article

Published Version

Ceilometer-Based Analysis of Shanghai's Boundary Layer Height (under Rain- and Fog-Free Conditions)

JIE PENG,[a,b] C. S. B. GRIMMOND,[c] XINSHU FU,[a,b] YUANYONG CHANG,[a,b] GUANGLIANG ZHANG,[d] JIBING GUO,[d] CHENYANG TANG,[d] JIE GAO,[e] XIAODONG XU,[f] AND JIANGUO TAN[a,b]

[a] *Shanghai Institute of Meteorological Science, Shanghai Meteorological Service, Shanghai, China*
[b] *Shanghai Key Laboratory of Meteorological and Health, Shanghai Meteorological Service, Shanghai, China*
[c] *Department of Meteorology, University of Reading, Reading, United Kingdom*
[d] *Fengxian Meteorological Service, Shanghai Meteorological Service, Shanghai, China*
[e] *Shanghai Central Meteorological Observatory, Shanghai Meteorological Service, Shanghai, China*
[f] *Department of Integrated Observations and Forecasting, Shanghai Meteorological Service, Shanghai, China*

(Manuscript received 30 June 2016, in final form 13 January 2017)

ABSTRACT

To investigate the boundary layer dynamics of the coastal megacity Shanghai, China, backscatter data measured by a Vaisala CL51 ceilometer are analyzed with a modified ideal curve fitting algorithm. The boundary layer height z_i retrieved by this method and from radiosondes compare reasonably overall. Analyses of mobile and stationary ceilometer data provide spatial and temporal characteristics of Shanghai's boundary layer height. The consistency between when the ceilometer is moving and stationary highlights the potential of mobile observations of transects across cities. An analysis of 16 months of z_i measured at the Fengxian site in Shanghai reveals that the diurnal variation of z_i in the four seasons follows the expected pattern; for all seasons z_i starts to increase at sunrise, reflecting the influence of solar radiation. However, the boundary layer height is generally higher in autumn and winter than in summer and spring (mean hourly averaged z_i for days with low cloud fraction at 1100–1200 local time are 900, 654, 934, and 768 m for spring, summer, autumn, and winter, respectively). This is attributed to seasonal differences in the dominant meteorological conditions, including the effects of a sea breeze at the near-coastal Fengxian site. Given the success of the retrieval method, other ceilometers installed across Shanghai are now being analyzed to understand more about the spatial dynamics of z_i and to investigate in more detail the effects of prevailing mesoscale circulations and their seasonal dynamics.

1. Introduction

The depth of the atmospheric boundary layer (BL), or the lowest part of the atmosphere that directly interacts with Earth's surface (Stull 1988), can vary from meters to 2–3 km. Given the exchanges of momentum, heat, moisture, and other substances between Earth's surface and atmosphere occur in this layer, its depth is an important control on the volume of air in which pollutants disperse. Consequently, knowledge of the depth of the BL z_i (for a list of variables, see Table A1) is important for a broad range of applications, including weather forecasts, and aviation safety, as well as atmospheric diffusion and air quality.

Traditionally, z_i has been determined from thermodynamic profiles measured by radiosondes (Bond 1992; Zeng et al. 2004; Guo et al. 2016). However, their temporal resolution is poor (two to three operational launches per day) even during intensive observation periods (<10 per day) (Seibert et al. 2000). Hence, radiosonde-derived z_i do not capture the full diurnal surface heating cycle (Liu and Liang 2010). Alternative methods use different wavelengths of sound (sodar, wind profilers), radio (radar) (e.g., Bianco and Wilczak 2002) and light (lidar) (e.g., Grimsdell and Angevine 1998) to determine the characteristics of the boundary layer. Lidars measure the backscatter from atmospheric constituents, such as aerosols (e.g., Melfi et al. 1985; Steyn et al. 1999; Brooks 2003; Eresmaa et al. 2006; Tsaknakis et al. 2011; Wang et al. 2012; Sawyer and Li 2013). As aerosol concentrations are generally greater in the BL than the free atmosphere above, the change in aerosol backscatter with height can be used to retrieve z_i. As ceilometers are designed to determine cloud-base height from the vertical

Corresponding author e-mail: Prof. Jianguo Tan, tanjg@mail.typhoon.gov.cn

DOI: 10.1175/JTECH-D-16-0132.1

aerosol backscatter profiles, they have the potential to yield data on z_i and have the advantage that they can operate unattended in all weather conditions.

The height of the capping inversion layer, or the top of the residual layer (RL), is another critical height that differentiates the lowest part of atmosphere from the free atmosphere (see Stull 1988, Fig. 1.7). As the RL typically forms in the late afternoon, decoupled from the mixing layer, it also contains more aerosols than the free atmosphere. Thus, the height with the largest decrease in aerosol concentration may actually be related to an RL, z_{RL}, which may be above the z_i. Given the location, depth, and number of RLs impact the degree of radiative cooling (Blay-Carreras et al. 2014), it is an important characteristic of the lower atmosphere. In this paper, z_i refers to the height with a large decrease of aerosol concentration, but it is replaced with z_{RL} if there is sufficient evidence to indicate that it is z_{RL} rather than z_i.

The objective of this paper is to analyze ceilometer data to assess the spatial and temporal characteristics of Shanghai's z_i. First, a methodology is developed based on the ideal curve fit algorithm (Steyn et al. 1999) with a wavelet covariance transform (Sawyer and Li 2013). The new method allows the initial parameters to be obtained in a manner that is suitable for automatic retrieval of z_i in large datasets. Further modifications allow for atmospheric conditions with aerosol layers in the lower troposphere. The results are compared with z_i retrieved from radiosondes. Ceilometer data are then analyzed for a mobile traverse across Shanghai and from one urban site for the period May 2013–August 2014. Through analysis of the spatial and temporal boundary layer characteristics of this coastal megacity, valuable information for weather and/or air quality forecasts is provided.

2. Data and methodology

a. Observations

A Vaisala CL51 ceilometer (firmware: V1031) was used to collect backscatter profiles up to 4500-m range with 10-m resolution averaged for each 16 s. The instrument was installed at Fengxian meteorological station (FX; 30.93°N, 121.48°E; Fig. 1) from 14 May 2013 to 26 August 2014 (350 days). Power supply issues caused a loss of data in spring (number of days available by month—2013 May/June: 11/14, respectively; 2014 April/May/June: 30/6/15, respectively) and to a lesser extent in summer (2013 July/August/September: 13/19/25, respectively; 2014 June/July/August: 15/31/26, respectively). Thus, some statistics should be interpreted with caution. The $z_{i,ceil}$ is retrieved from these data using the methods presented in section 2b.

A traverse across Shanghai, from Fengxian Bay to Shidongkou (Fig. 1), was conducted from 0445 to 2305 local time (LT) 27 July 2013. A van with both the ceilometer and a ZQZ-CY automatic weather station, mounted at the back and middle, undertook an alternating sequence of 30-min mobile and 30-min stationary measurements. Observations from the last 15 min (~60 backscatter coefficient profiles) of each stationary period were compared with those from the first 15 min of the next mobile period, and between the first 15 min of a stationary period and the last 15 min of the prior mobile period. This allowed for differences in performance related to the motion of the vehicle to be assessed.

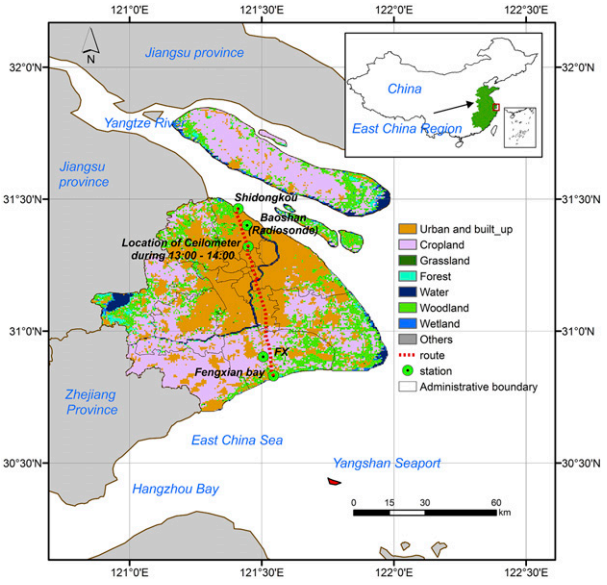

FIG. 1. Mobile traverse route (red dashed line) taken on 27 Jul 2013 from Shidongkou, Baoshan, to the location of the ceilometer (between 1300 and 1400 LT), and Fengxian. Sites are marked by green circles. The land use of Shanghai (in 2011) is derived from the MODIS land cover type product (MCD12Q1; Friedl et al. 2010).

Radiosonde profiles of temperature, humidity, and pressure (10-m vertical resolution) are regularly gathered in Shanghai using GTS1 digital radiosondes (Shanghai Changwang Meteotech Co. 2015). The radiosondes are released at the Baoshan District Meteorological Office (Baoshan; 31.40°N, 121.45°E; Fig. 1) at 0715, 1315, and 1915 LT. These profiles are used to derive $z_{i,sonde}$ using the methods described in section 2c.

b. Derivation of z_i from ceilometer data

Methods to retrieve z_i from lidar-observed backscatter include using a threshold as an indicator (Melfi et al. 1985); height of the largest negative gradient ($z_{i,grd}$); wavelet covariance transforms (Brooks 2003); ideal curve fitting (ICF) (Steyn et al. 1999); and combined algorithms based on wavelet covariance transforms and ICF (Sawyer and Li 2013). In this study a modified version of the Steyn et al. (1999) curve fitting method is used.

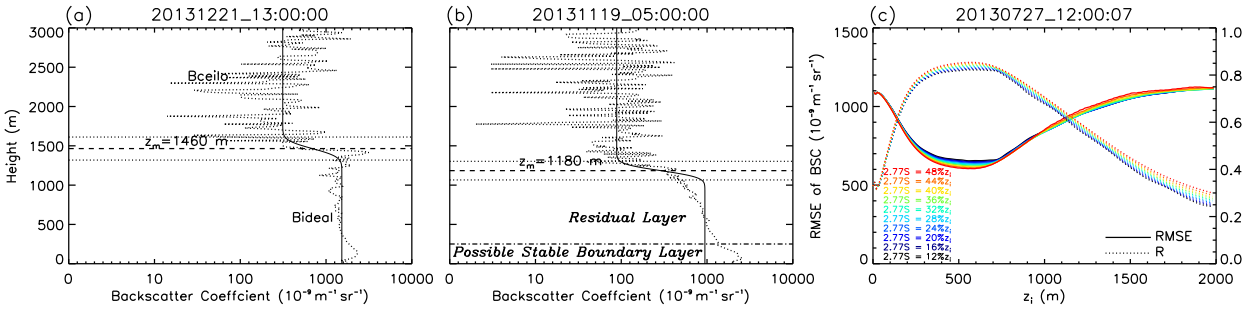

FIG. 2. (a) Backscatter coefficient profile (β, β_{ceil}, vertical dotted line) and corresponding best-fitted ideal curve (β_{ideal}, vertical solid line) measured at 1300:00 LT 21 Dec 2013. The $z_{i,\text{icf}}$ is equal to z_m (1460 m, horizontal dashed line). (b) Backscatter coefficient profile measured at 0500:00 LT 19 Nov 2013 when a notable residual layer appears. The top of the possible mixing layer is marked with a horizontal dashed–dotted line. (c) Variation of the correlation coefficient R and RMSE between measured β and the fitted ideal curve on z_i and S for the backscatter measured at 1200:07 LT 27 Jul 2013. Once z_i is obtained, S is determined (assuming 2.77S equal to 12%–50% of z_i with a step of 2%), the fitted ideal curve is determined, and R and RMSE are calculated.

Steyn et al. (1999) fit an ideal curve to the observed backscatter coefficient β profile to obtain $z_{i,\text{icf}}$:

$$\beta(z) = \frac{(\beta_m + \beta_u)}{2} - \frac{(\beta_m - \beta_u)}{2}\,\text{erf}\left(\frac{z - z_{i,\text{icf}}}{S}\right), \quad (1)$$

where β_m and β_u are the mean of the backscatter values for the boundary layer and the lower free troposphere, respectively. The depth of the sigmoid curve between β_m and β_u is related to S (Steyn et al. 1999), and $z_{i,\text{icf}}$ is the center of the transition zone and the retrieved boundary layer height. Simulated annealing (e.g., Press et al. 1992, 444–445) is used to iteratively determine the parameters in Eq. (1) simultaneously, based on the minimum root-mean-square error (RMSE) between the idealized curve and the backscatter profile (Fig. 2a). Although this iterative method is robust (Kirkpatrick et al. 1983), the quality of the results depends on the initial estimates (e.g., $z_{i,\text{icf}}$, β_m, β_u). However, for long-term automatic retrieval of $z_{i,\text{icf}}$, no single initial estimate is appropriate for the entire time series. To address this issue, Sawyer and Li (2013), who obtained an initial z_i ($z_{i,\text{icf}}$) from wavelet covariance transform for the curve fitting process, limited the range for iteration to permit the simulated annealing to find a best-fit curve to make the algorithm applicable to long-term datasets.

Following Sawyer and Li (2013), an automatic method is used in this study to find the initial height of z_i to reduce the likelihood of selecting a local solution. The procedure uses all heights from the first ceilometer gate (10 m) to 2 km (10-m step) to determine the RMSE. As z_i is generally lower than 2 km (Stull 1988), this height is used rather than 4500 m (the height of the available data) to reduce the algorithm calculation time significantly.

As S is not independent of β_m and β_u when determining z_i, the impact of S on the retrieved z_i was assessed. This assumed the entrainment zone (the region that aerosol concentration changes sharply for an RL situation) encompasses 95% of the depth of the sigmoid part of the curve (the region between the two horizontal dotted lines in Fig. 2a), has a depth of 2.77S (Steyn et al. 1999) and is equal to 12%–50% of the depth of z_i (evaluated using 2% steps). Given this, z_i was set and S was calculated. This allows β_m and β_u to be calculated. The goodness-of-fit statistics (RMSE, correlation coefficient R) are then calculated between β_{ideal} and β_{ceil} to enable their impact on S to be assessed (Fig. 2c). Generally, there is a convex (concave) relation with an increase of z_i to R (RMSE). The impact of changes in S (for the same initial z_i) results in very small changes in RMSE (and R) (Fig. 2c). This indicates that the thickness of the entrainment zone specified has a relatively small impact on the retrieved z_i compared to the choice of the initial z_i. These results are consistent with Steyn et al. (1999, see their Fig. 3).

Therefore, once z_i is determined, an entrainment zone equal to 20% of the depth of z_i is assumed. Thus S, β_m, and β_u are determined, and the curve is fitted. The minimum RMSE (β_{ceil}, β_{ideal}) is chosen as the best fit and the corresponding $z_{i,\text{icf}}$ is retrieved. Although this modification requires the algorithm to run nearly 200 times per backscatter profile, it is easily done because the computing time is very short. Given the algorithm for z_i retrieval used in this work is basically done by curve fitting step by step with all available initial heights, it is referred to as Step-IC (S-IC). A β profile may have features that are significantly different from ideal. When it rains, high β may extend from the cloud base to the surface (Fig. 3e). In the current study, all rainy days (128, as determined by the hourly rainfall record at FX) are removed because the structure of the boundary layer is modified by the rain. With no clear vertical decrease of β, the algorithm is not suitable. Fog and severe haze (initially identified visually by high backscatter coefficients close to the surface, confirmed by

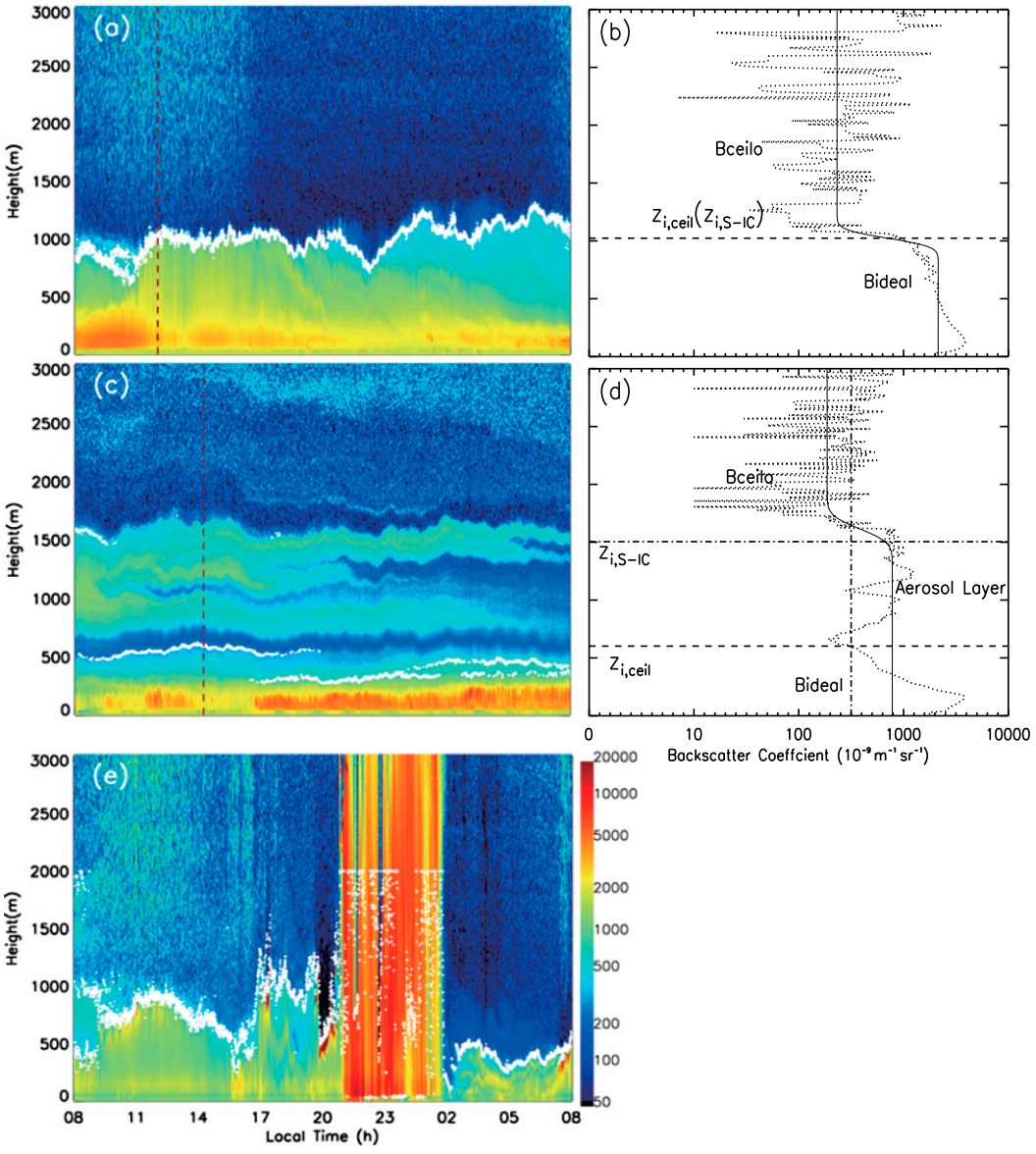

FIG. 3. Ceilometer backscatter coefficient and $z_{i,\mathrm{ceil}}$ (white diamond) for days that are (a) clear (24 h from 0800 LT 29 Dec 2013), (c) high aerosol (11 Sep 2013), and (e) rainy (24 h from 0800 LT 13 Sep 2013). (b),(d) Individual backscatter profiles (corresponding to vertical dotted red line in (a),(c), respectively) from one time (1319:44, 0133:08 LT, respectively) on each day and the fitted best ideal curve (vertical solid line) by Step-IC. Terms $z_{i,\mathrm{S\text{-}IC}}$ (horizontal dashed dotted line) and $z_{i,\mathrm{ceil}}$ (horizontal dashed line) are defined as the z_i directly retrieved by Step-IC and the one after aerosol examination process, respectively.

humidity and the visibility-based meteorological phenomena record for the Fengxian meteorological office) also alter the structure of the boundary layer, usually associated with the shallowest boundary layers, and yield β profiles not suitable for the S-IC analysis. These are classified as nontypical (NT) days and are also removed from the analysis. Therefore, the climatological analysis is for rain- and fog-free conditions. Although the $z_{i,\mathrm{icf}}$ can be retrieved for individual nonrainy β profiles on a day with rain, they are removed to avoid the impact of significantly varying boundary layer structures on rainy day. Thus, the categories of β profiles identified for analysis are clear (CL) and aerosol layer (AL) conditions (Fig. 3).

CL conditions occur when there is no rainfall or other weather phenomena that would alter the vertical structure of aerosol concentration significantly. Consequently, the vertical distribution of the corresponding β has a shape most similar to the ''ideal'' pattern

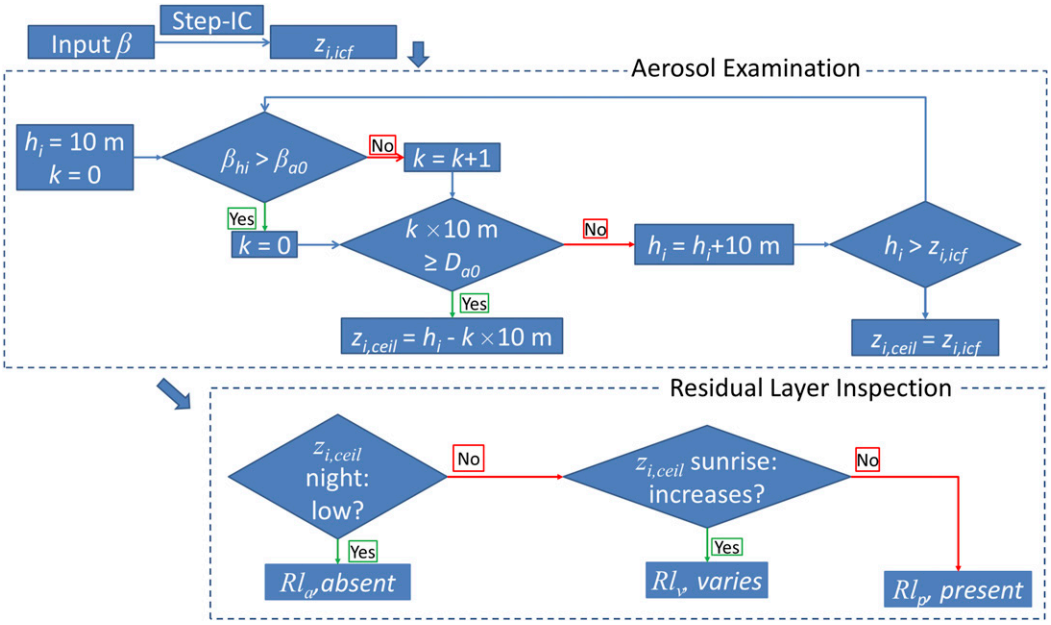

FIG. 4. Flowchart of Step-IC with aerosol processing and residual layer inspection. First, Step-IC is applied to each individual backscatter coefficient profile β to retrieved $z_{i,\mathrm{icf}}$. Second, aerosol examination determines whether multiple aerosol layers exist. If present, $z_{i,\mathrm{icf}}$ is set to the top of lowest aerosol layer, and after examination ($z_{i,\mathrm{ceil}}$). Third, subjective residual layer inspection based on nocturnal values and the variation of $z_{i,\mathrm{ceil}}$ at sunrise. Other notation: h_i:height tracked for determination of the gap between multiple aerosol layers; k: number of continuous layers with backscatter coefficient smaller than backscatter of a typical aerosol layer; β_{hi}: backscatter coefficient at height of h_i; β_{a0}: backscatter coefficient of typical aerosol layer ($3.162 \times 10^{-7}\,\mathrm{m^{-1}\,sr^{-1}}$); D_{a0}: threshold of distance to define a gap between multiple aerosol layers (100 m).

(Figs. 3a,b). The method should perform best under these conditions.

If aerosol layers appear, then the β profile has multiple peaks and a multilayer structure in the time–height cross section of β (Fig. 3c). The retrieved z_i would be the top of the layer with the largest change of β. However, as the top of the lowest layer actually reflects the height that the concentration of aerosols from the surface reduces significantly for the first time, this is designated as the z_i.

An analysis of the mean β when aerosols were present ($\beta_{\mathrm{a0}} = 3.162 \times 10^{-7}\,\mathrm{m^{-1}\,sr^{-1}}$) in layers was undertaken for 5 days to aid automated detection. To ensure the profile is multilayered, a threshold distance between aerosol layers (D_{a0} = 100 m) was set. First, the β profiles are analyzed from the surface to identify any region with backscatter continuously less than β_{a0} and with a vertical range larger than D_{a0}. If present, it is assumed that a multilayer β profile structure exists. The first height h_a with a β less than β_{a0} is $z_{i,\mathrm{ceil}}$. Aerosol layers may be dynamic and therefore layers may vary in time. Currently, each profile is treated independently and layers are not tracked. This is an avenue for future improvements in the approach (e.g., Parikh and Parikh 2002; Kotthaus et al. 2016). The representativeness threshold values (β_{a0}, D_{a0}) obviously impact the results. If the β_{a0} is too small (large), then the multilayer feature will be missed (overselected), resulting in a z_i that is overestimated (underestimated). Similarly, if D_{a0} is too small (large), then too many (few) layers will be detected and thus z_i will tend to be underestimated (overestimated). Therefore, these threshold values must be appropriate for the region of interest. With the aerosol examination process, the algorithm is applicable to more complex conditions (Fig. 4 gives a flowchart of the method).

In Shanghai under cloudy conditions, the β from cloud droplets is generally much larger than that from aerosols, because the aerosols are mostly in the fine mode (Cheng et al. 2015) and the wavelength of the laser ceilometer used for measurement is 905 ± 10 nm (Kotthaus et al. 2016). To identify the cloudy profiles, a threshold β for clouds (β_{c0}) was used to detect the presence of clouds at any height within the range of ceilometer measurement (4500 m). After examination of β profiles for cloud conditions during the study period (β increases significantly at the cloud base; but rate would start to reduce slightly above the cloud base, which indicates clouds present the mean β at that height for many clouds were selected as β_{c0}), which was set to $10^{-5}\,\mathrm{m^{-1}\,sr^{-1}}$. As the scattering properties of typical clouds will vary with location and season, a regionally specific value probably needs to be determined. If β_{c0} is set too large, then cloud with β smaller

TABLE 1. Summary of consistency of z_i determined from analyzes of 575 radiosondes released from Baoshan BS (14 May 2013–31 Mar 2014). See section 2c for details.

	Good	Relatively good—θ, q	Relatively good—θ, RH	Relatively good—q, RH	Possible—θ, θ
Variables > threshold	θ, q, RH	θ, q	θ, RH	q, RH	θ, θ
Reliability level	1	2	2	3	4
Number of cases	22	19	69	316	149

than β_{c0} will not be identified. Conversely, if β_{c0} is too small, then z_i with β larger than β_{c0} (such as in heavily polluted conditions) would be falsely classified as cloud.

Rather than using the manual observations. Cloud fraction is estimated from the ceilometer profiles. The fraction of time with cloud cover f_c each day can be determined using

$$f_c = (N_c/N_{\text{total}}) \times 100, \tag{2}$$

where N_c and N_{total} are the number of profiles with cloud and total profiles for each measured day, respectively. The N_{total} may vary for an individual day if a complete set of observations is unavailable.

Of the 222 days with no rain, 185 have continuous ceilometer measurements from 0000 to 2400 LT; 45 of these are NT days. Thus, 140 days are available for the climatological analysis (section 3c). These are subdivided into clear (32 days), cloudy (108 days), and aerosol layer (5 days) days. Note that aerosol layer days are also clear or cloudy days.

c. Derivation of z_i from radiosonde data

To determine z_i from radiosonde vertical profiles of temperature and humidity, two methods are used. The first requires user judgment of the base of an elevated temperature inversion layer or the height of a significant reduction in moisture (i.e., a "subjective" method), often accompanied by wind shear (Seibert et al. 2000). If no clear moisture reduction or inversion layer is found, it is hard to determine the z_i.

The second approach uses the bulk Richardson number R_b. This is a commonly used method (Seibert et al. 2000) that determines the surface R_{bs} (Vickers and Mahrt 2004) from

$$R_{\text{bs}}(z_R) = z_R \left(\frac{g}{\overline{\theta}}\right) \frac{[\theta(z_R) - T_s]}{U(z_R)^2}, \tag{3}$$

where g is the gravitational acceleration, $\theta(z_R)$ is the potential temperature at height z_R, T_s is the near-surface air temperature, $U(z_R)$ is the wind speed at z_R, and $\overline{\theta}$ is the mean potential temperature between the surface and z_R. In this study, temperature at 10 m (the lowest level of radiosonde data) is used for T_s. The other variables are calculated from the radiosonde profile data. Usually, $z_{i,\text{sonde}}$ is assigned the first height when $R_{\text{bs}} >$ a critical Richardson number R_c (Zilitinkevich and Baklanov 2002). The value of R_c can be dynamic, across a relatively large range (see Table 2 in Zilitinkevich and Baklanov 2002), and may depend on surface roughness. To evaluate R_c, sensitivity tests were undertaken with respect to the z_i, determined. Although uncertainties occur in both methods, we consider the results to be more reliable when there is closer agreement between the two methods.

The subjective (user judgment) method is based on the interpretation of radiosonde potential temperature θ and specific humidity q, calculated from the temperature T, relative humidity RH, and pressure P profiles:

1) A threshold for the vertical gradient (S) of θ, q, and RH (S_θ, S_q, S_{rh}, respectively) is required to determine the height with large variation of temperature and humidity. If the threshold is too small, then the results are impacted by noise; if it is too large, then z_i may not be found. After inspecting a large number of radiosonde profiles, S_θ, S_q, and S_{rh} were set to 1 K (50 m)$^{-1}$, 0.001 kg kg^{-1} (50 m)$^{-1}$, and 3% (50 m)$^{-1}$, respectively.
2) Working from the surface to higher layers, the first height with a vertical gradient of $\theta > 0.5$ K (50 m)$^{-1}$ (again, based on analysis of a large amount data) is defined as h_{P1}. Therefore, h_{P1} is the first height that θ changes are relatively large.
3) If any two of S_θ, S_q, and S_{rh} for any layer within 100 m of h_{P1} exceed the threshold, indicating both temperature and humidity have large changes near h_{P1}, then this is defined as $z_{i,\text{rs}}$. With three variables that could exceed the threshold (but only two needed to retrieve $z_{i,\text{rs}}$) the reliability of retrieved $z_{i,\text{rs}}$ changes with conditions. These are classified into *Good*—θ, q, and RH all exceed the threshold; or *Relatively Good*—θ, q; *Relatively Good*—θ, RH; or *Relatively Good*—q, RH (where θ and q, or θ and RH, or q and RH exceed the threshold, respectively).
4) If no layer within 100 m of h_{P1} exceeds the threshold, then the first height (h_{P2}) with θ 1 K > mean θ between the surface and 100 m ($\overline{\theta}_{0\text{–}100\text{m}}$) is targeted. If the distance between h_{P1} and h_{P2} is <100 m, then h_{P1} is considered as $z_{i,\text{rs}}$ and the retrieved $z_{i,r}$ are considered to have the lowest reliability ("Possible—θ, θ").

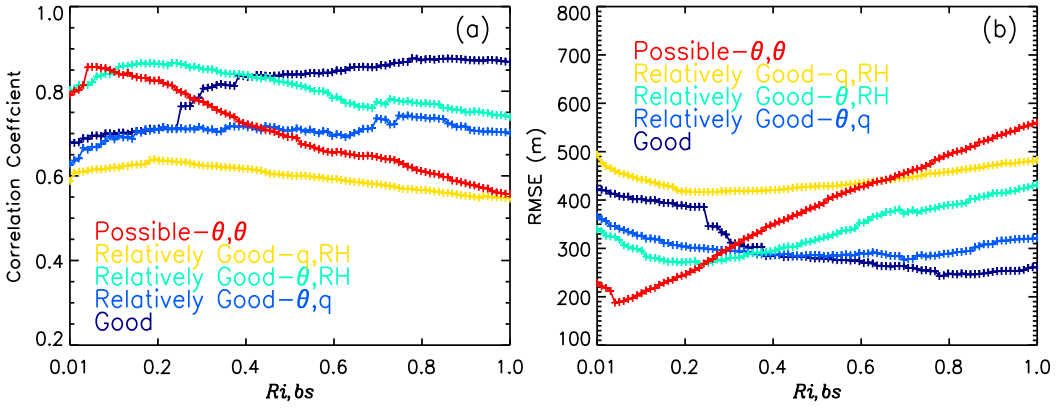

FIG. 5. Evaluation metrics (a) correlation coefficient R and (b) RMSE for $z_{i,\mathrm{rs}}$ determined by subjective interpretation (section 2c) of radiosonde data (potential temperature θ, relative humidity RH, and specific humidity q) and by objective surface bulk Richardson number ($\mathrm{Ri_{bs}}$) method. Categories are defined in Table 1.

If no heights satisfy the above-mentioned criteria, then this method does not retrieve $z_{i,\mathrm{rs}}$.

For each of the 575 Baoshan radiosonde ascents analyzed (Table 1), the objective bulk Richardson number method ($z_{i,\mathrm{Ri}}$) was applied with R_c varying from 0.01 to 1.0 (step of 0.01). From statistical analysis (R, RMSE) between $z_{i,\mathrm{rs}}$ and $z_{i,\mathrm{Ri}}$ (Fig. 5), the "Good" category (deep blue) variation is used to set R_c for this study. Given the increase of R (decrease of RMSE) until R_c is close to 0.4 (and little change thereafter), this value is chosen. This R_c is used with all available radiosonde data and Eq. (3) to obtain the $z_{i,\mathrm{sonde}}$ used to evaluate $z_{i,\mathrm{ceil}}$ from the ceilometers (section 3b).

An analysis of differences between the subjective and objective z_i do not suggest that there is any other consistent basis (e.g., wind direction, time of day, wind speed) to modify the R_c values, so one constant value is

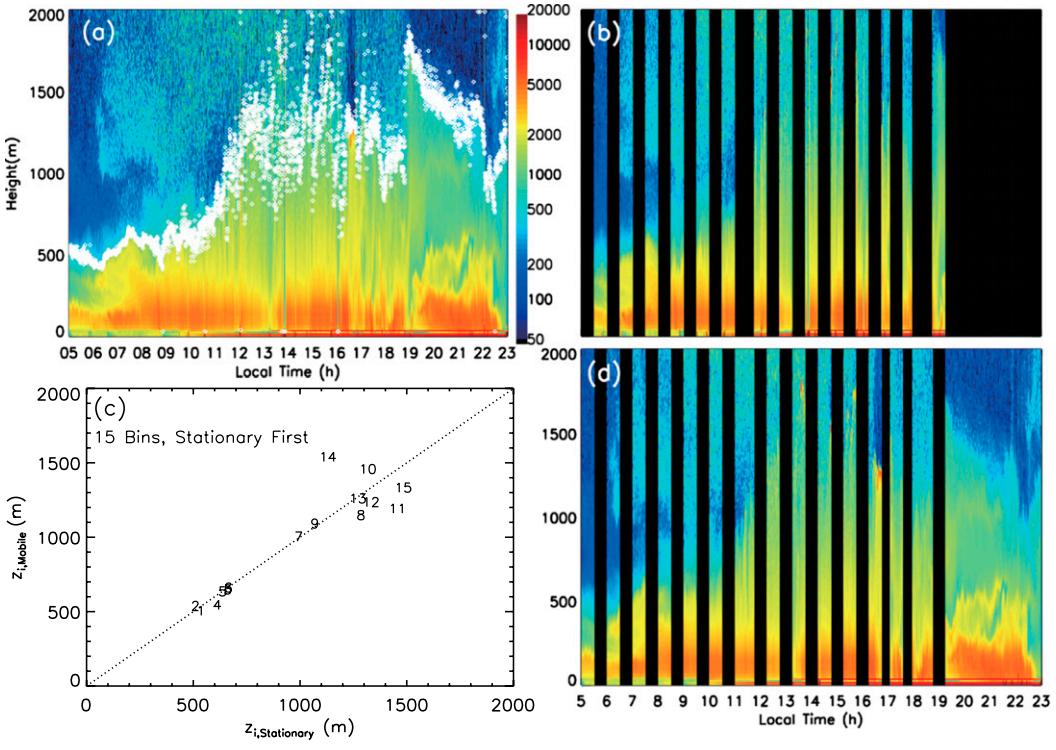

FIG. 6. Characteristics of Shanghai boundary layer on 27 Jul 2013 as observed by a traverse (Fig. 1) (a) time–height cross section of backscatter β, and the retrieved $z_{i,\mathrm{ceil}}$ (white diamond, section 2b)-observed β when ceilometer was (b) moving and (d) stationary; and (c) group mean $z_{i,\mathrm{ceil}}$ between observations when the vehicle was in motion and stationary (number indicates the sequence of each compared group in 15 sequential pairs; see section 3a).

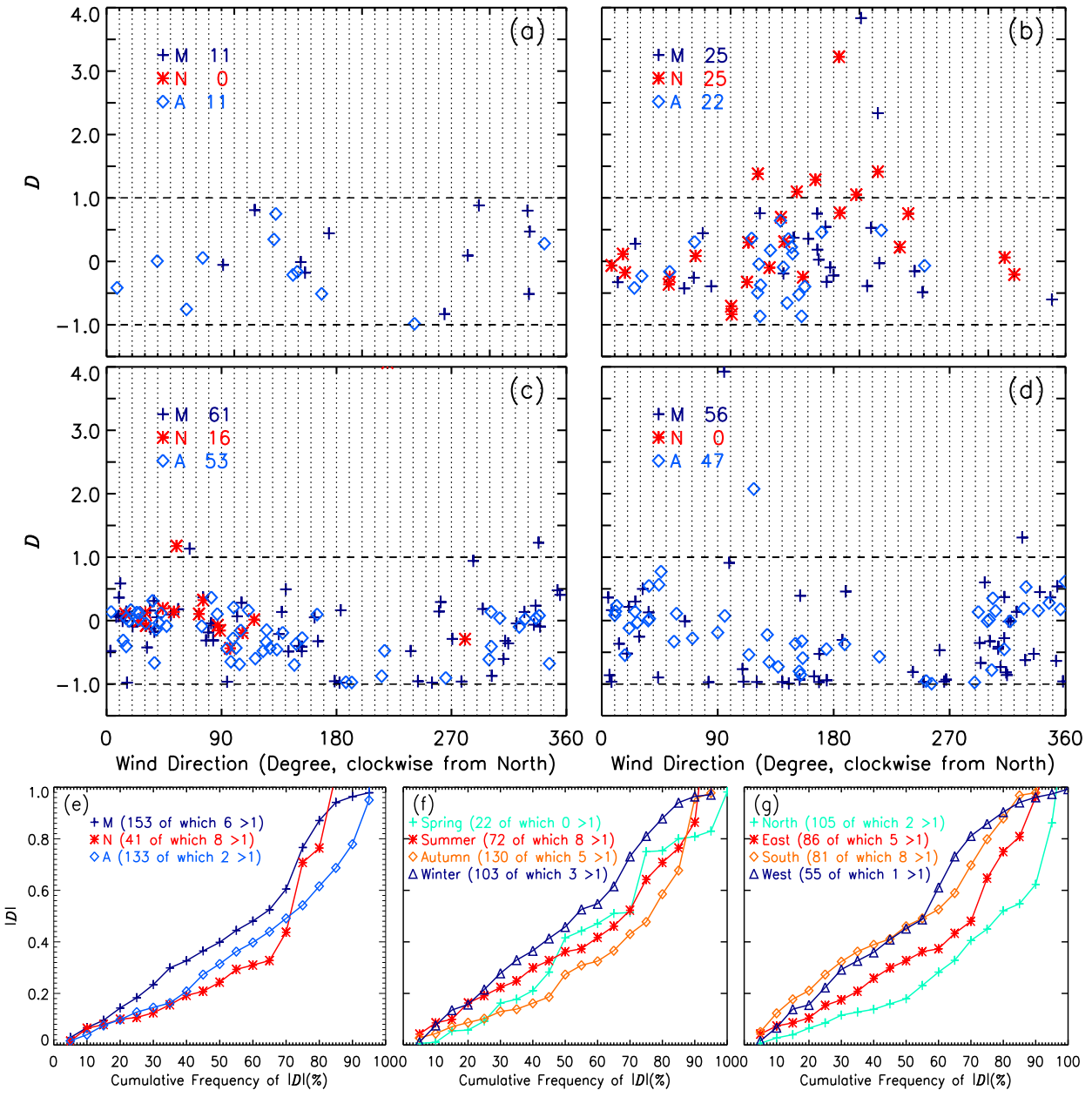

FIG. 7. Normalized difference D [Eq. (4)] between $z_{i,\mathrm{ceil}}$ and $z_{i,\mathrm{sonde}}$ as a function of wind direction in (a) spring, (b) summer, (c) autumn, and (d) winter. Cumulative proportion of absolute value of D (for $|D| > 1$ numbers indicated) by (e) time of day: morning (M, 0715 LT), midday (N, 1315 LT), and late afternoon (A, 1915 LT); (f) season; and (g) wind direction (north: 0–45 and 315–360, east: 45–135, south: 135–225, west: 225–315). Numbers in plot indicate amount of data available.

used. There is evidence that the differences are smaller between $z_{i,\mathrm{subjective}}$ ($z_{i,\mathrm{rs}}$) and $z_{i,\mathrm{objective}}$ ($z_{i,\mathrm{Ri}}$) in spring/summer than in winter/autumn (not shown). The poorest performance occurs for the Good category in autumn mornings when there is a systematic underestimation of $z_{i,\mathrm{objective}}$ ($z_{i,\mathrm{rs}}$) relative to $z_{i,\mathrm{subjective}}$ ($z_{i,\mathrm{Ri}}$) when $R_c = 0.4$, whereas for all other seasons and times of day the reverse is true but with a much smaller difference. The RMSE for the Good category are 164.9, 96.5, 345.0, and 184.0 m in spring, summer, autumn, and winter, respectively.

3. Results

a. *Mobile observation*

To assess the spatial variability of boundary layer characteristics across Shanghai (Fig. 1), the time–height

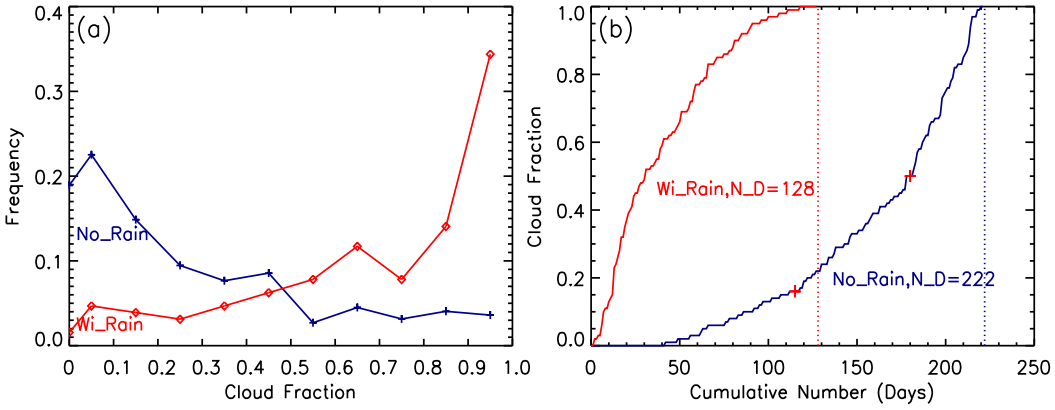

FIG. 8. Ceilometer-observed cloud fraction f_c (section 2b) for 14 May 2013–26 Aug 2014 with (Wi_Rain, red) and without rain (No_Rain, blue) determined from hourly rainfall at FX. (a) Proportion of total number of days (N = 350) by cloud fraction f_c and (b) cumulative frequency of f_c. Two red crosses mark the threshold to distinguish three classes of no-rain cloud conditions.

cross section of ceilometer-measured β on the traverse day (27 July 2013) and the $z_{i,\text{ceil}}$ retrieved by S-IC are presented in Fig. 6. Both β and $z_{i,\text{ceil}}$ have the characteristics of a typical unstable summer boundary layer (Oke 1976). Before sunrise, $z_{i,\text{ceil}}$ is low with aerosols concentrated at low altitudes; after sunrise the aerosols are gradually lifted to higher levels as solar radiative heating increases turbulent heating; later in the day $z_{i,\text{ceil}}$ gradually decreases, increasing the aerosol concentrations at lower altitudes after sunset. The sudden jump of $z_{i,\text{ceil}}$ around 19 h is probably due to the proximity of a coastal chemical plant emitting a high concentration of pollution that is being detected by the ceilometer.

Comparing mean $z_{i,\text{ceil}}$ (Fig. 6c) from the 15 sequential pairs of mobile and stationary observations (i.e., two 15-min periods), the observed β are consistent (Figs. 6b,d). Mean $z_{i,\text{ceil}}$ for the last 30 min of each hour are also the same (not shown). This good agreement (mobile/stationary) highlights the potential for mobile transects across cities to study the spatial and temporal dynamics of the boundary layer.

b. *Comparison between the radiosonde and ceilometer results*

The availability of the radiosonde launches provides data to evaluate the ceilometer-based results. The $z_{i,\text{ceil}}$ from the FX ceilometer is compared to the Baoshan (BS) radiosonde $z_{i,\text{sonde}}$ for both the main (0715 and 1915 LT) and extra launch times (e.g., 1315 LT during the flood season of June–September). Mean $z_{i,\text{ceil}}$ for the periods 0700–0800, 1300–1400, and 1900–2000 LT are used, with a varying number per season (spring: 22, summer: 72, autumn: 130, and winter: 103).

The 56 km between FX and BS is mostly urban (Fig. 1), but there are likely differences in the boundary layer structure. As the wind direction differences alter the upwind surface characteristics of FX and BS (Fig. 1), the normalized difference (D) between $z_{i,\text{ceil}}$ and $z_{i,\text{sonde}}$ by wind direction for the four seasons was calculated to assess this:

$$D = \frac{z_{i,\text{ceil}} - z_{i,\text{sonde}}}{z_{i,\text{ceil}}}. \tag{4}$$

The mean radiosonde wind direction between 200 and 300 m above ground level was used (10° bins). There is generally good agreement [$|D| < 0.25$ (1.0) for ~40% (95%) profiles], given their differences (e.g., thermodynamic vs aerosol concentration profiles; noncollocation), between $z_{i,\text{ceil}}$ and $z_{i,\text{sonde}}$. The results vary with season (spring: MAM; summer: JJA; autumn: SON; winter: DJF) and wind direction (Fig. 7). Of the available cases in spring, summer, autumn, and winter $|D| < 0.25$ (0.5) [1.0] for 36.4%, 34.7%, 49.2%, and 26.2% (59.1%, 68.1%, 79.2%, and 51.5%) [100%, 88.9%, 96.2% and 97.1%], respectively. In summer and autumn, the highest agreement occurs when the wind direction is northerly or easterly. However, in winter the agreement is much weaker for easterly winds. The best performance (assessed by D value, which 50% of the data are less than or equal to) is midday (0.243; Fig. 7e) for the time of day, autumn (0.273; Fig. 7f) for season, and northerly (0.179; Fig. 7g) for wind directions. Similarly, the poorest agreement (using the same metric) occurs in the morning (0.398), in winter (0.458), and under southerly wind conditions (0.461). The southerly wind conditions are when BS will be much more influenced by the urban land surface, whereas FX is marine (Fig. 1). The typical diurnal processes cause the normalization in the morning to be probably using a smaller value; hence, the D values

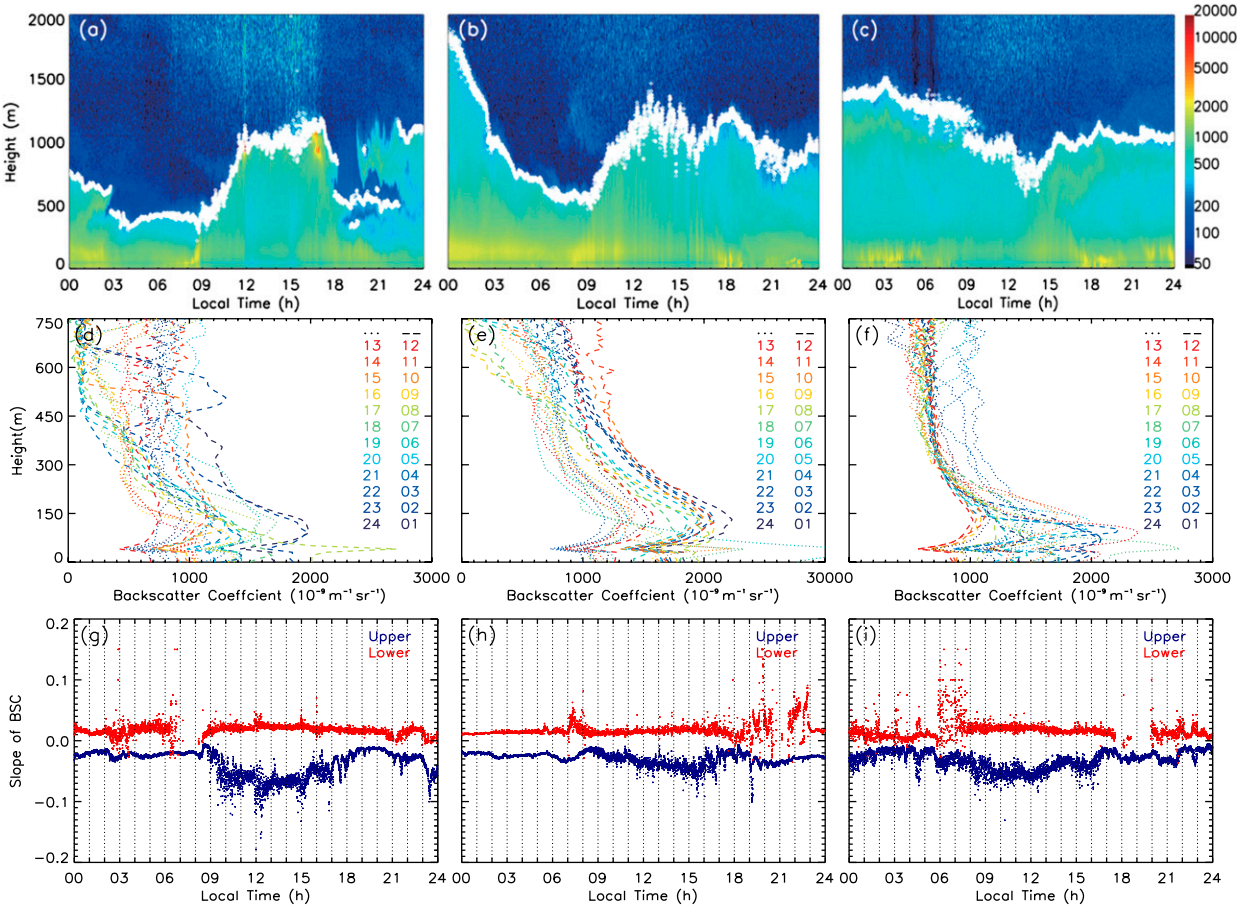

FIG. 9. Ceilometer backscatter coefficient β and $z_{i,\mathrm{ceil}}$ (white diamond) for examples of (a) residual layer absent RL_a (15 Feb 2014), (b) residual layer RL_v (28 Oct 2013), and (c) residual layer constantly present RL_p under clear skies (29 Nov 2013). Hourly (0100–2400 LT) β profiles between 0 and 750 m for (d) RL_a, (e) RL_v and (f) RL_p, dashed and dotted lines are used for first and second halves of the day, respectively. Two heights with significant variation of β can be seen (sharp decrease SD around 40 m; inflection point IP around 130 m); time series of linear fit slopes between SD and IP (S_{low}) and the slope between IP and 300 m (S_{up}) for (g) RL_a, (h) RL_v and (i) RL_p, respectively.

are expected to be potentially higher. Similarly, the higher values in winter may be impacted.

Given the potential mesoscale and local scale differences in the boundary layer structure caused by site differences and distance, the ceilometer backscatter analyzed by S-IC retrieve reasonable $z_{i,\mathrm{ceil}}$ values. Therefore, the climatology of $z_{i,\mathrm{ceil}}$ is analyzed (section 3c).

c. *Climatology of Shanghai's boundary layer height*

As the boundary layer development is strongly dependent on solar and turbulent heating, z_i varies with cloud cover and season. The mean daily cloud fraction f_c [Eq. (2)] for the entire study period is 0.42 (summer: 0.47, winter: 0.34). In summer, the mei-yu front rainy season (7–30 June 2013 and 20 June–7 July 2014), which is associated with the monsoon and south/southeast winds and an almost unlimited ocean moisture source, combined with the strong urban heat island, helps to enhance total cloud cover. In winter, drier air masses affect the city, mainly derived from the north, leading to lower cloud cover.

When stratified by rain conditions (Fig. 8: days are binned by cloud fraction from $0 < f_c \leq 0.1$ to $0.9 < f_c \leq 1.0$ with an interval of 0.1), there is the expected high percentage of low (high) f_c for nonrain (rain) days. Of the dry days, the change in slope for increasing f_c (Fig. 8b) is used to split the data into four cloud cover classes: clear (0), little (0.01–0.160), medium (0.161–0.50), and large (0.501–1.0). The 140 dry days with measurements are classified by f_c [type 1 (TI): clear to little, type 2 (T2): medium to large] and season. To have sufficient data for statistical analysis of $z_{i,\mathrm{ceil}}$, only two f_c classes are used to enable seasonal analysis (especially in spring).

Frequently, $z_{i,\mathrm{ceil}}$ retrieved in the morning and after sunset is located at the top of an overlying RL rather than being a mixing or stable boundary layer below

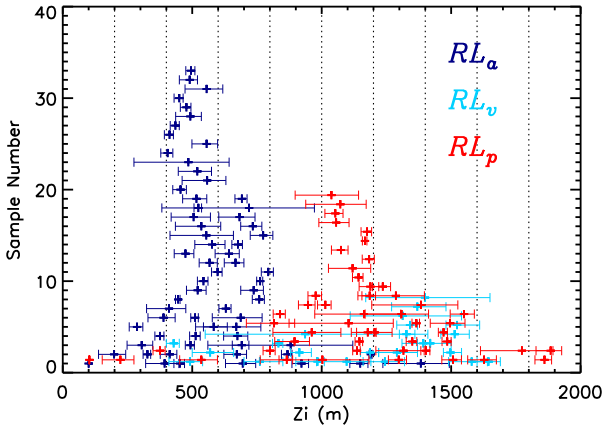

FIG. 10. The mean (+) and interquartile IQR range of $z_{i,\mathrm{ceil}}$ between 0000 LT and sunrise for each day color coded by RL class (absent, variable, and present). Frequency (y axis) is based on each day being classified based on the mean z_i into 200-m bins.

(Fig. 2b). As the $z_{i,\mathrm{ceil}}$ essentially is the height with the largest variation of β (section 1), we could only roughly classify the retrieved $z_{i,\mathrm{ceil}}$ as the top of boundary layer (RL) if its value is small (high) in the nighttime (Fig. 4). Even without an RL it is difficult to be certain the top of an aerosol layer is the boundary layer height. Visual inspection of all 140 days suggest the results can be split into three classes (Fig. 9): 1) $z_{i,\mathrm{ceil}}$ is barely impacted by the presence of RL, as throughout the day the BL is retrieved (RL$_a$, absent); 2) high $z_{i,\mathrm{ceil}}$ values at night suggest they probably represent the z_{RL} but the boundary layer growth in the morning is as expected theoretically, indicating daytime retrieval is good (RL$_v$, varies); and 3) high nocturnal $z_{i,\mathrm{ceil}}$ values indicate they are z_{RL} with the height remaining large throughout the day, so diurnal variability is difficult to determine (e.g., growth of the BL) (RL$_p$, present).

To investigate the objectivity of this classification, the mean and interquartile (IQR) of $z_{i,\mathrm{ceil}}$ between midnight (0000 LT) and sunrise for each case are considered (Fig. 10): 1) for RL$_a$ cases, $z_{i,\mathrm{ceil}}$ generally have a small mean and IQR, which is consistent with the expected low and likely stable boundary layer at night; 2) for RL$_p$ cases, $z_{i,\mathrm{ceil}}$ are generally large and with relative narrow IQR, indicating the presence of a consistently deep RL through the night; 3) the large variation of $z_{i,\mathrm{ceil}}$ for RL$_v$ cases corresponds well with a decrease of $z_{i,\mathrm{ceil}}$ in the night/early morning (Fig. 9b). However, it is important to note that even for RL$_a$ cases, RL may be present but indistinguishable from shallow nocturnal boundary layer at night and lead to an overestimate of $z_{i,\mathrm{ceil}}$ that could be further investigated if nocturnal radiosonde were available. The frequency of the three types varies through the year (Table 2) with most RL$_v$ and most RL$_p$ days in the autumn and winter. A priori this seasonal pattern is expected: without strong growth of the convective boundary layer, residual layers are likely to be retained.

TABLE 2. Number of days in the three RL classes (RL$_a$, RL$_v$, RL$_p$) (see section 3c) subdivided by cloud fraction condition (T1 and T2) of the 140 analyzed days. See Fig. 9.

	RL$_a$		RL$_p$		RL$_v$	
Period	T1	T2	T1	T2	T1	T2
Spring	6	5	2	0	1	0
Summer	13	17	2	1	4	1
Autumn	7	8	7	4	14	9
Winter	7	4	5	3	17	3
Year	33	34	16	8	36	13
Total	67		24		49	

To consider the processes below the RL, the lower part of the backscatter (β) profiles (Figs. 9d–f) through a day are explored. The profiles from their lowest point have 1) a consistent sharp decrease (SD) of β close to the surface (40 m above the ceilometer) that corresponds with known problems [incomplete optical overlap correction, low-level obstruction correction, and hardware-related perturbation, as described by Kotthaus et al. (2016)]; 2) relatively consistent inflection points (IP) at around 130 m (but time varying); and 3) a slope of β between the IP and upper layer (about 300 m) that changes with time. The change in slope relates to vertical variation in aerosol concentration and is indicative of the vertical mixing processes.

From the time series (Figs. 9g–i) of the two slopes [IP to 300 m (S_{up}); SD to IP (S_{low})], it is evident that 1) S_{low} are more consistent than S_{up}; 2) large changes in both occur in the morning and late afternoon; and 3) the morning changes of S_{up} occur earlier in autumn (0600 LT 28 Oct 2013, 0645 LT 29 Nov 2013) than winter (0815 LT 15 Feb 2014) in response to the potential initiation of mixing from solar forcing. Given the changes of vertical mixing in the morning (late afternoon) generally indicate the time that z_i starts to increase (decrease), this finding provides a potential way to differentiate the retrieved $z_{i,\mathrm{ceil}}$ from z_{RL} and z_i. This will be explored further in future work.

The diurnal variation of Shanghai's $z_{i,\mathrm{ceil}}$ for three classes and four seasons (Fig. 11) show clear differences as expected. For RL$_a$ cases (Figs. 11a,b) four main features consistent with theory (Stull 1988) are evident: a relatively consistent $z_{i,\mathrm{ceil}}$ during the night; $z_{i,\mathrm{ceil}}$ increases after sunrise, associated with solar radiative heating that enhances vertical turbulence and moves the aerosols higher into the atmosphere; the largest $z_{i,\mathrm{ceil}}$ occur in the late afternoon; and $z_{i,\mathrm{ceil}}$ then decreases gradually after sunset. For RL$_p$ cases (Figs. 11e,f), the $z_{i,\mathrm{ceil}}$ remains relatively constant through the morning through to the middle of

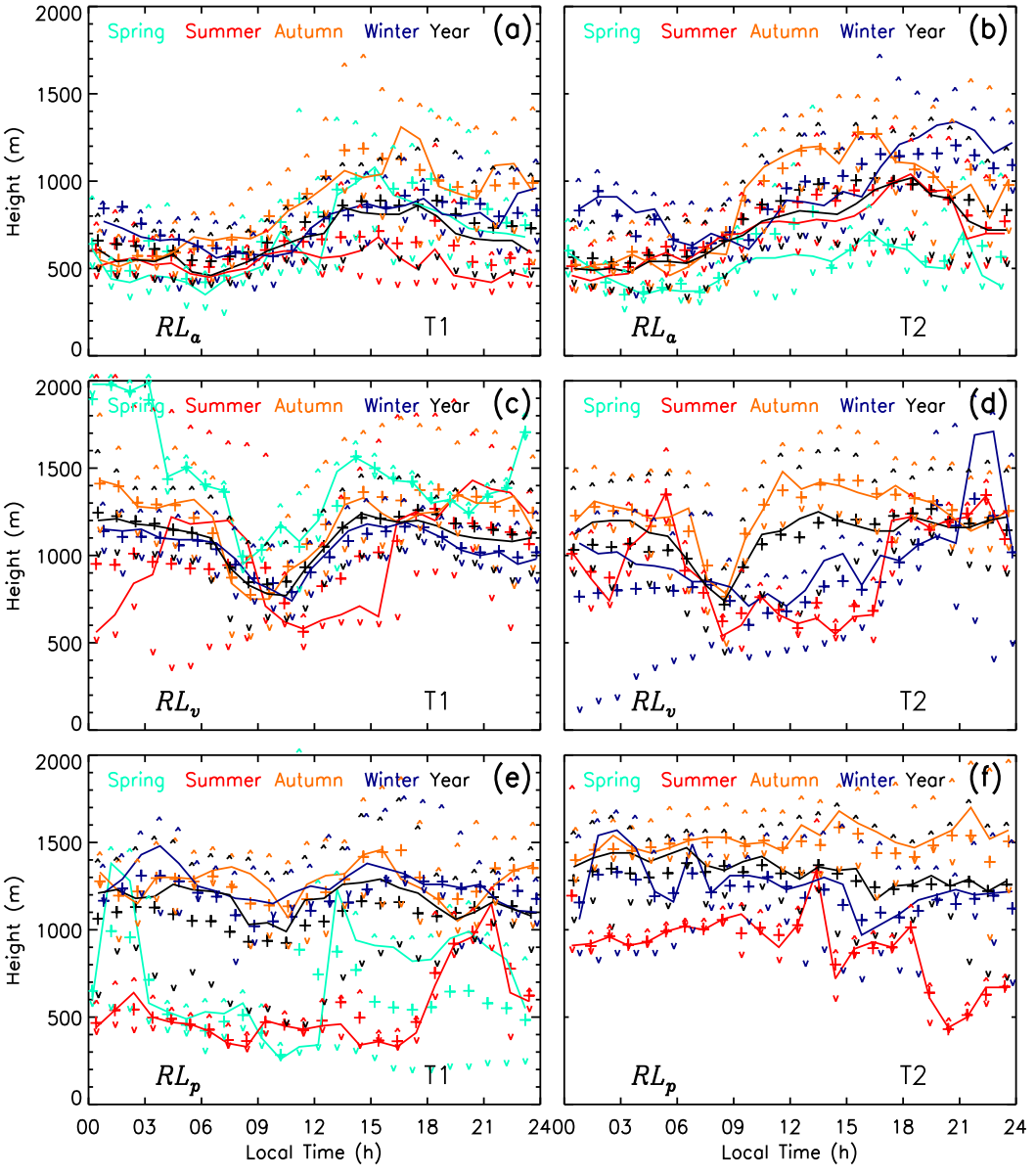

FIG. 11. Ceilometer-determined BL height or RL top height [$z_{i,c}$; Eq. (1) diurnal median (solid line), mean (+) and IQR (75%: ^, 25%: v] stratified by seasons, f_c [Eq. (2)] (T1 and T2), and residual layer condition: (a),(b) RL_a; (c),(d) RL_v; and (e),(f) RL_p.

the day, but for the RL_v cases (Figs. 11c,d) a very sharp decrease of $z_{i,\mathrm{ceil}}$ occurs in the morning. Therefore, for the RL_v cases, the residual layer tends to disappear as the mixing layer grows in the morning.

Seasonal differences in $z_{i,\mathrm{ceil}}$ under RL_a conditions are largest in autumn, and decrease from winter and spring to summer. To explore these potentially unexpected results, the meteorological measurements at the FX site are investigated. Just 9.6 km from the sea (Fig. 1), the area experiences distinct circulation patterns that vary with season. The relation between daily maximum z_i and surface wind direction when z_i generally starts to grow (0700 LT shown, a similar pattern occurs 0600–0900 LT), relative humidity at 0700 LT (when relative humidity starts to decrease), and the average wind speed between 0800 and 1200 LT (the period of greatest z_i growth) measured at the FX site for the 30 summer and 15 autumn RL_a cases are shown in Fig. 12. In summer, the morning predominant wind direction (across Shanghai) is from the south or southeast, off the nearby ocean. This, along with high humidity (relative humidity $> 80\%$), is expected to lead to a lower z_i. In

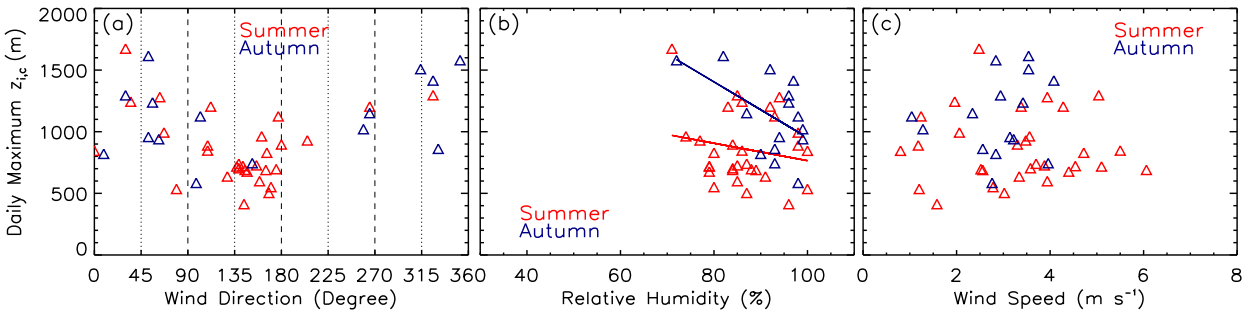

FIG. 12. Observed variation in summer and autumn daily maximum $z_{i,c}$ and other variables measured at FX (based on ceilometer observations using S-IC) for RL_a cases as a function of (a) wind direction (at 10 m) at 0700 LT, (b) RH at 0700 LT (at 1.5 m) with linear regression lines to show the trend, and (c) mean wind speed between 0800 and 1200 LT.

addition, during the mei-yu front period (9–16 July 2013, 14 June–11 July 2014) there is a large increase in cloud cover and precipitation, which also reduces z_i.

In the autumn, solar heating remains large (Ao et al. 2016a) but with a dominant wind direction (at 10 m at 0700) for most days from the west and north (i.e., from the mainland instead of the sea). The morning boundary layer growth is slightly enhanced by this relatively drier warmer air with lower wind speeds, resulting in higher z_i in autumn than in summer. The mean of the daily maximum z_i for days with wind from between 130 and 170° (main direction a sea breeze would impact FX) in summer (14 days) and relative humidity less than 90% in autumn (4 days) of RL_a cases are 680 and 1291 m, respectively.

The local time at which the boundary layer starts to grow in Shanghai varies with season and is significantly earlier in summer (0700 LT for both types 1 and 2) than in winter (0900 and 1000 LT for types 1 and 2, respectively). This corresponds closely with the time of sunrise, reflecting the significant influence of solar radiation on $z_{i,\mathrm{ceil}}$. The growth rate of z_i for RL_a cases from near sunrise (summer 0450–0530 LT, autumn 0530–0630 LT) to midday and the mean z_i in the midday (1100–1200 LT) was determined from the hourly mean z_i for each day (Table 3). Consistent with the results above, both the growth rate and midday mean of z_i in autumn are larger than in summer because of the dominant seasonal weather conditions. For spring and winter, the growth rates are higher for type 1 than for type 2. Relatively high growth rates in spring for both types 1 and 2 cases are due to the expected large sensible heat fluxes (Ao et al. 2016b).

Other studies of coastal urban areas (e.g., Seidel et al. 2010; Melecio-Vázquez et al. 2015; Niyogi et al. 2015) have found z_i to be lower in summer than that in autumn. Seidel et al. (2010), for example, explained their findings in terms of subsidence inversions associated with the Pacific high pressure system, which dominates in the summer off the coast. Niyogi (2015) demonstrated a similar summertime reduction z_i in Miami, Florida, and Brookhaven, New York, from an analysis of twice daily soundings over 10 years. He attributed this to a stronger vertical temperature gradient that enhances the intrusion and mixing of sea-breeze air, which reduces the growth. Melecio-Vázquez et al.'s (2015) analysis of the maximum vertical gradient of potential temperature and relative humidity measured by a microwave radiometer (Radiometrics MP-3000A) in New York, also found lower z_i in summer when relative humidity gradients are the metric. However, this is not the case if potential temperatures are used, when they are marginally the largest in the middle of the day.

TABLE 3. Morning growth rate (m h^{-1}) and midday (1100–1200 LT) mean height (m) of z_i for days with RL_a (see section 3c for data classification) for the two cloud classes (T1 and T2) by season. Period of morning analyzed: spring and summer: 0500–1200 LT and autumn and winter: 0600–1200 LT. See Table 2 for the number of days.

	T1					T2				
	Morning growth rate (m h^{-1})				Midday Mean z_i	Morning growth rate (m h^{-1})				Midday Mean z_i
	Mean	Median	Minimum	Maximum	(m)	Mean	Median	Minimum	Maximum	(m)
Spring	72.0	90.8	4.1	142.9	900.3	66.5	25.9	14.5	186.9	674.3
Summer	38.8	32.8	12.7	87.0	654.1	51.9	47.1	7.2	132.2	814.5
Autumn	66.8	65.4	24.4	108.3	934.4	93.6	100.6	22.7	166.2	1052.
Winter	82.9	88.7	51.7	108.2	698.0	54.4	51.4	5.8	127.7	958.8
Year	60.1	51.0	4.1	142.9	767.7	64.2	55.0	7.2	186.9	866.8

TABLE A1. The names, units, and descriptions of symbols and abbreviations.

Variable	Unit	Description
β	$m^{-1}\ sr^{-1}$	Backscatter coefficient
β_{a0}	$m^{-1}\ sr^{-1}$	Mean β when aerosol present
β_{c0}	$m^{-1}\ sr^{-1}$	β threshold for the identification of cloud
β_{ceil}	$m^{-1}\ sr^{-1}$	β observed by ceilometer
β_{hi}	$m^{-1}\ sr^{-1}$	β at height of hi (see Fig. 4)
β_{ideal}	$m^{-1}\ sr^{-1}$	β of the ideal curve
β_m	$m^{-1}\ sr^{-1}$	Mean β for the boundary layer
β_u	$m^{-1}\ sr^{-1}$	Mean β for the lower free troposphere
θ	K	Potential temperature
$\overline{\theta}$	K	Mean θ between the surface and height z_R
$\theta(z_R)$	K	θ at height of z_R
$\overline{\theta}_{0–100m}$	K	Mean θ between the surface and 100 m
AL	—	Aerosol layer
BL	—	Boundary layer
BS	—	Baoshan site
CL	—	Clear
D	—	Normalized difference
D_{a0}	m	Threshold of distance to define a gap between multiple aerosol layers
f_c	%	Mean daily cloud fraction
FX	—	Fengxian meteorological station
g	$m\ s^{-1}$	Gravitational acceleration
h_a	m	First height with β smaller than β_{a0}
h_{p1}	m	First height with vertical gradient of $\theta > 0.5$ K $(50\ m)^{-1}$
h_{p2}	m	First height with θ 1 K $> \overline{\theta}_{0–100m}$
ICF	—	Ideal curve fitting algorithm
IP	—	Relatively consistent inflection points
IQR	—	Interquartile range
NT	—	Nontypical days
N_c	—	Number of profiles with cloud for each measured days
N_{total}	—	Number of total profiles for each measured days
P	hPa	Air pressure profile from radiosonde
q	$kg\ kg^{-1}$	Specific humidity
R	—	Correlation coefficient
R_b	—	Bulk Richardson number
R_{bs}	—	Surface bulk Richardson number
R_c	—	Critical Richardson number
RH	%	Relative humidity
RL	—	Residual layer
RL_a	—	Residual layer absent
RL_p	—	Residual layer present
RL_v	—	Residual layer varies
RMSE	—	Root-mean-square error
S	m	Depth of the sigmoid curve in the fitted best curve
SD	—	Sharp decrease of β close to the surface
S-IC	—	Step ideal curve fitting algorithm
S_{low}	$m^{-1}\ sr^{-1}\ m^{-1}$	Slope of β between SD and IP
S_q	$kg\ kg^{-1}\ m^{-1}$	Threshold for vertical gradient of q
S_{rh}	$\%\ m^{-1}$	Threshold for vertical gradient of RH
S_{up}	$m^{-1}\ sr^{-1}\ m^{-1}$	Slope of β between IP and 300 m
S_θ	$K\ m^{-1}$	Threshold for vertical gradient of θ
T	K	Temperature
T_s	K	Temperature at surface
$U(z_R)$	$m\ s^{-1}$	Wind speed at z_R
z_i	m	Boundary layer height
$z_{i,ceil}$	m	z_i retrieved by ceilometer using S-IC and after aerosol examination process
$z_{i,grd}$	m	z_i retrieved based on the largest negative gradient of β
$z_{i,icf}$	m	z_i retrieved by ICF

TABLE A1. (*Continued*)

Variable	Unit	Description
$z_{i,\mathrm{Ri}}$ ($z_{i,\mathrm{objective}}$)	m	z_i retrieved by radiosonde using Richardson number (objective) method
$z_{i,\mathrm{rs}}$ ($z_{i,\mathrm{subjective}}$)	m	z_i retrieved by radiosonde using subjective method
$z_{i,\mathrm{sonde}}$	m	z_i retrieved by radiosonde
z_R	m	Height z_R
z_{RL}	m	z_i retrieved by ceilometer using S-IC but related to be the top of a residual layer

4. Conclusions

Shanghai's boundary layer height (z_i) height is determined for the period 14 May 2013–26 August 2014 from data retrieved from ceilometer backscatter using a modified curve fitting method (S-IC) and radiosondes. The seasonal characteristics are analyzed using the more continuous ceilometer data. From this work, we conclude the following:

- The proposed modified ideal curve fit algorithm S-IC allows long-term z_i automatic retrieval, but the results may relate to the top of the residual layer when present (not always the mixed layer).
- A comparison with radiosonde-derived data shows that the ceilometer algorithm has an acceptable performance [differences are within <25% (100%) of each other approximately 40% (95%) of all the compared cases], considering these are not collocated observations, so they will occasionally have real differences in z_{RL}.
- The hourly mean maximum z_i is larger in autumn/winter than spring/summer. An analysis of meteorological data reveals this pattern can be attributed to seasonal differences in the dominant air mass and onshore flows at the near-coastal FX site. Such seasonal patterns have been documented elsewhere.
- The good agreement of the ceilometer's performance (mobile/stationary) assessed during an across-Shanghai observation highlights the potential to study the boundary layer's spatial and temporal dynamics in Shanghai and/or other cities using mobile ceilometer observations.

Given the success of the S-IC method, other ceilometers installed across Shanghai will be analyzed to understand more about the spatial dynamics of the z_i across a megacity and to investigate in more detail the effects of prevailing mesoscale circulations.

Acknowledgments. This work was supported by the National Natural Science Foundation of China (Grant 41275021), the Met Office/Newton Fund CSSP-China, the China Clean Development Mechanism Fund Grants Program (Grant 2012043), and the Shanghai Science and Technology Committee Research Project (Grant 16ZR1431700). The authors thank the Vaisala Corporation for its support.

APPENDIX

List of Variables

Variables used in the paper are presented in Table A1.

REFERENCES

Ao, X., C. S. B. Grimmond, D. Liu, Z. Han, P. Hu, Y. Wang, X. Zhen, and J. Tan, 2016a: Radiation fluxes in a business district of Shanghai, China. *J. Appl. Meteor. Climatol.*, **55**, 2451–2468, doi:10.1175/JAMC-D-16-0082.1.

——, and Coauthors, 2016b: Heat, water and carbon exchanges in the tall megacity of Shanghai: Challenges and results. *Int. J. Climatol.*, **36**, 4608–4624, doi:10.1002/joc.4657.

Bianco, L., and J. M. Wilczak, 2002: Convective boundary layer depth: Improved measurement by Doppler radar wind profiler using fuzzy logic methods. *J. Atmos. Oceanic Technol.*, **19**, 1745–1758, doi:10.1175/1520-0426(2002)019<1745:CBLDIM>2.0.CO;2.

Blay-Carreras, E., and Coauthors, 2014: Role of the residual layer and large-scale subsidence on the development and evolution of the convective boundary layer. *Atmos. Chem. Phys.*, **14**, 4515–4530, doi:10.5194/acp-14-4515-2014.

Bond, N. A., 1992: Observations of planetary boundary layer structure in the eastern equatorial Pacific. *J. Climate*, **5**, 699–706, doi:10.1175/1520-0442(1992)005<0699:OOPBLS>2.0.CO;2.

Brooks, I. M., 2003: Finding boundary layer top: Application of a wavelet covariance transform to lidar backscatter profiles. *J. Atmos. Oceanic Technol.*, **20**, 1092–1105, doi:10.1175/1520-0426(2003)020<1092:FBLTAO>2.0.CO;2.

Cheng, T., and Coauthors, 2015: Seasonal variation and difference of aerosol optical properties in columnar and surface atmospheres over Shanghai. *Atmos. Environ.*, **123**, 315–326, doi:10.1016/j.atmosenv.2015.05.029.

Eresmaa, N., A. Karppinen, S. M. Joffre, J. Rasane, and H. Talvitie, 2006: Mixing height determination by ceilometer. *Atmos. Chem. Phys.*, **6**, 1485–1493, doi:10.5194/acp-6-1485-2006.

Friedl, M. A., D. Sulla-Menashe, B. Tan, A. Schneider, N. Ramnakutty, A. Sibley, and X. Huang, 2010: MODIS Collection 5 global land cover: Algorithm refinements and characterization of new datasets. *Remote Sens. Environ.*, **114**, 168–182, doi:10.1016/j.rse.2009.08.016.

Grimsdell, A. W., and W. M. Angevine, 1998: Convective boundary layer height measurement with wind profilers and comparison to cloud base. *J. Atmos. Oceanic Technol.*, **15**, 1331–1338, doi:10.1175/1520-0426(1998)015<1331:CBLHMW>2.0.CO;2.

Guo, J. P., and Coauthors, 2016: The climatology of planetary boundary layer height in China derived from radiosonde and reanalysis data. *Atmos. Chem. Phys.*, **16**, 13 309–13 319, doi:10.5194/acp-16-13309-2016.

Kirkpatrick, S., C. D. Gelatt Jr., and M. P. Vecchi, 1983: Optimization by simulated annealing. *Science*, **220**, 671–680, doi:10.1126/science.220.4598.671.

Kotthaus, S., E. O'Connor, C. Münkel, C. Charlton-Perez, M. Haeffelin, A. M. Gabey, and C. S. B. Grimmond, 2016: Recommendations for processing atmospheric attenuated backscatter profiles from Vaisala CL31 ceilometers. *Atmos. Meas. Tech.*, **9**, 3769–3791, doi:10.5194/amt-9-3769-2016.

Liu, S., and X.-Z. Liang, 2010: Observed diurnal cycle climatology of planetary boundary layer height. *J. Climate*, **23**, 5790–5809, doi:10.1175/2010JCLI3552.1.

Melecio-Vázquez, D., J. González-Cruz, M. Arend, Z. Han, E. Gutierrez, M. Dempsey, and J. Booth, 2015: New York metro-area boundary layer catalogue: Boundary layer height and stability conditions from long-term observations. *Ninth Int. Conf. on Urban Climate/12th Symp. on the Urban Environment*, Toulouse, France, IAUC and Amer. Meteor. Soc., 9-2. [Available online at http://www.meteo.fr/icuc9/presentations/NOMTM/NOMTM9-2.pdf.]

Melfi, S. H., J. D. Spinhirne, and S. H. Chou, 1985: Lidar observations of the vertically organized convection in the planetary boundary layer over the ocean. *J. Climate Appl. Meteor.*, **24**, 806–821, doi:10.1175/1520-0450(1985)024<0806:LOOVOC>2.0.CO;2.

Niyogi, D., 2015: Urban impacts on regional rainfall climatology. *Ninth Int. Conf. on Urban Climate/12th Symp. on the Urban Environment*, Toulouse, France, IAUC and Amer. Meteor. Soc., UCP9-7. [Available online at http://www.meteo.fr/icuc9/presentations/UCP/UCP9-7.pdf.]

Oke, T. R., 1976: The distinction between canopy and boundary-layer urban heat islands. *Atmosphere*, **14**, 268–277.

Parikh, N. C., and J. A. Parikh, 2002: Systematic tracking of boundary layer aerosols with laser radar. *Opt. Laser Technol.*, **34**, 177–185, doi:10.1016/S0030-3992(01)00107-4.

Press, W. H., S. A. Teukolsky, W. T. Vettering, and B. R. Flannery, 1992: *Numerical Recipes in FORTRAN: The Art of Scientific Computing*. 2nd ed. Cambridge University Press, 933 pp.

Sawyer, V., and Z. Li, 2013: Detection, variations and intercomparison of the planetary boundary layer depth from radiosonde, lidar and infrared spectrometer. *Atmos. Environ.*, **79**, 518–528, doi:10.1016/j.atmosenv.2013.07.019.

Seibert, P., F. Beyrich, S.-E. Gryning, S. Joffre, A. Rasmussen, and P. Tercier, 2000: Review and intercomparison of operational methods for the determination of the mixing height. *Atmos. Environ.*, **34**, 1001–1027, doi:10.1016/S1352-2310(99)00349-0.

Seidel, D. J., C. O. Ao, and K. Li, 2010: Estimating climatological planetary boundary layer heights from radiosonde observations: Comparison of methods and uncertainty analysis. *J. Geophys. Res.*, **115**, D16113, doi:10.1029/2009JD013680.

Shanghai Changwang Meteotech Co., 2015: GTS1 digital radiosonde. Accessed 10 June 2015. [Available online at http://www.cwqx.com/product_h/radiosonde.htm.]

Steyn, D. G., M. Baldi, and R. M. Hoff, 1999: The detection of mixed layer depth and entrainment zone thickness from lidar backscatter profiles. *J. Atmos. Oceanic Technol.*, **16**, 953–959, doi:10.1175/1520-0426(1999)016<0953:TDOMLD>2.0.CO;2.

Stull, R. B., 1988: *An Introduction to Boundary Layer Meteorology*. Kluwer Academic 666 pp.</Bok>

Tsaknakis, G., A. Papayannis, P. Kokkalis, V. Amiridis, H. D. Kambezidis, R. E. Mamouri, G. Georgoussis, and G. Avdikos, 2011: Inter-comparison of lidar and ceilometer retrievals for aerosol and Planetary Boundary Layer profiling over Athens, Greece. *Atmos. Meas. Tech.*, **4**, 1261–1273, doi:10.5194/amt-4-1261-2011.

Vickers, D., and L. Mahrt, 2004: Evaluating formations of stable boundary layer height. *J. Appl. Meteor.*, **43**, 1736–1749, doi:10.1175/JAM2160.1.

Wang, Z., X. Cao, L. Zhang, J. Notholt, B. Zhou, R. Liu, and B. Zhang, 2012: Lidar measurement of planetary boundary layer height and comparison with microwave profiling radiometer observation. *Atmos. Meas. Tech.*, **5**, 1965–1972, doi:10.5194/amt-5-1965-2012.

Zeng, X., M. A. Brunke, M. Zhou, C. Fairall, N. Bond, and D. H. Lenschow, 2004: Marine atmospheric boundary layer height over the eastern Pacific: Data analysis and model evaluation. *J. Climate*, **17**, 4159–4170, doi:10.1175/JCLI3190.1.

Zilitinkevich, S., and A. Baklanov, 2002: Calculation of the height of the stable boundary layer in practical applications. *Bound.-Layer Meteor.*, **105**, 389–409, doi:10.1023/A:1020376832738.